VIP Composite Materials Very Important Paper

Deutsche Ausgabe: DOI: 10.1002/ange.201606870
Internationale Ausgabe: DOI: 10.1002/anie.201606870

Combining Nitrogen-Doped Graphene Sheets and MoS_2: A Unique Film–Foam–Film Structure for Enhanced Lithium Storage

Ting-Tian Shan[+], Sen Xin[+], Ya You[+], Huai-Ping Cong, Shu-Hong Yu,* and Arumugam Manthiram*

Abstract: *With a notable advantage in terms of capacity, molybdenum disulfide has been considered a promising anode material for building high-energy-density lithium-ion batteries. However, its intrinsically low electronic conductivity and unstable electrochemistry lead to poor cycling stability and inferior rate performance. We herein describe the scalable assembly of free-standing MoS_2–graphene composite films consisting of nitrogen-doped graphene and ultrathin honeycomb-like MoS_2 nanosheets. The composite has a unique film–foam–film hierarchical top-down architecture from the macroscopic to the microscopic and the nanoscopic scale, which helps rendering the composite material highly compact and leads to rapid ionic/electronic access to the active material, while also accommodating the volume variation of the sulfide upon intercalation/deintercalation of Li. The unique structural merits of the composite lead to enhanced lithium storage.*

Lithium ion batteries (LIBs) have been powering modern electronics since their emergence in the early 1990s.[1] To further improve the energy output of such batteries, recent efforts have been focused on the use of novel non-intercalation electrode materials with larger capacities, such as sulfur cathodes and sulfide anodes, to replace conventional intercalation-type cathode (e.g., $LiCoO_2$) and anode (e.g., graphite) materials. Molybdenum disulfide (MoS_2), a typical transition-metal sulfide, has been considered a promising anode material for LIBs owing to its two-dimensional, layered S-Mo-S sandwich structure and numerous active sulfur sites, which enable Li storage in a two-step process, namely by a typical insertion route followed by a conversion reaction to generate Li_2S and Mo at the end of the initial discharge. As a result, it offers a theoretical specific capacity that is twice (ca. 670 $mA\,h\,g^{-1}$) as large as that of graphite.[2] However, the intrinsically low electronic conductivity of the sulfide and the unstable sulfur electrochemistry after the initial charge process lead to poor cycling stability and inferior rate performance. Furthermore, the restacking of cycled MoS_2 layers into bulk materials upon charging hinders its complete lithiation/delithiation, which significantly deteriorates its performance.

Against these drawbacks, the combination of nanostructured MoS_2 with conductive carbon has been shown to be an effective strategy to improve the electrochemical performance. With nano-MoS_2 uniformly dispersed on carbon components with highly exposed active sites and large specific surface areas, the ionic and electronic conductivities can be significantly improved, and the electrochemistry can be stabilized by sulfide pinning on carbon or strong interactions between the sulfide and carbon components, so that the restacking of sulfide can be prevented.[3] Among carbon matrices, graphene is especially attractive owing to its large specific surface area, high electronic conductivity, and high flexibility, and is used as an ideal substrate for the assembly of nano-MoS_2 for use as LIB anodes.[4]

The construction of hierarchically structured MoS_2–graphene composite materials, particularly by the assembly of MoS_2 nanosheets on three-dimensional (3D) graphene architectures, appears to be a further promising approach to improve lithium storage.[5] The key to achieving such properties lies in building a MoS_2–graphene composite with an optimal micro/nanoarchitecture, which should combine favorable electrochemical stability with fast electrode kinetics; the density of the composite should also be taken into consideration so that a high energy density can be ensured. Based on this concept, we herein describe the rational design and scalable assembly of free-standing MoS_2–graphene composite films consisting of N-doped graphene and ultrathin honeycomb-like MoS_2 nanosheets (NG–MoS_2) by reduction with hydrazine vapor followed by a facile hydrothermal procedure. The composite has a unique hierarchical film–foam–film (3F) top-down architecture from the macro- to the micro- and the nanoscale. When used as an anode material for LIBs, the composite displayed a high tap density, and Li^+/e^- could rapidly access the active material. Furthermore, the composite structure helped accommodate the volume variation upon Li intercalation/deintercalation into/from the sulfide. The 3F NG–MoS_2 composite delivered a high specific capacity and

[*] T.-T. Shan,[+] Dr. S. Xin,[+] Prof. H.-P. Cong
School of Chemistry and Chemical Engineering
Hefei University of Technology
Hefei 230009 (P.R. China)
E-mail: hpcong@hfut.edu.cn
Prof. S.-H. Yu
Division of Nanomaterials & Chemistry
Hefei National Laboratory for Physical Sciences at the Microscale
Collaborative Innovation Center of Suzhou Nano Science and Technology, CAS Center for Excellence in Nanoscience
Department of Chemistry
University of Science and Technology of China
Hefei 230026 (P.R. China)
E-mail: shyu@ustc.edu.cn
Dr. Y. You,[+] Prof. A. Manthiram
Materials Science and Engineering
The University of Texas at Austin
Austin, TX 78712 (USA)
[+] These authors contributed equally to this work.
Supporting information and the ORCID identification number(s) for the author(s) of this article can be found under: http://dx.doi.org/10.1002/anie.201606870.

energy output, while also showing excellent cyclability and rate capability when used in a LIB.

The synthesis of the 3F MoS_2–graphene film started with the evaporation-induced assembly of a graphene oxide (GO) dispersion with dissolved $(NH_4)_6Mo_7O_{24}$ in a Teflon mold (Figure 1a; see also the Supporting Information, Figure S1a) to form a compact, molybdate-containing GO film with an average thickness of approximately 25 μm (Figure S2). After chemical reduction of the GO film with hydrazine vapor,

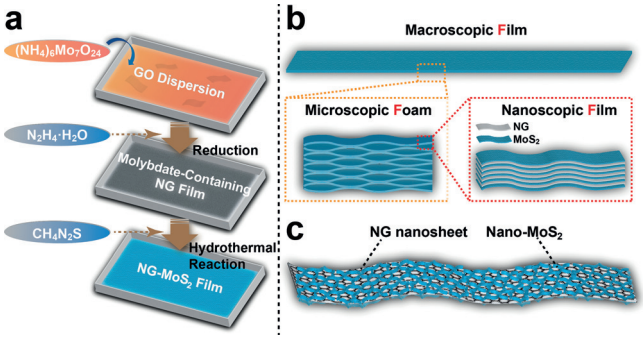

Figure 1. a) Preparation of NG–MoS_2. b) The 3F hierarchical structure of NG–MoS_2. c) The typical sandwich structure of a NG nanosheet with nano-MoS_2 coated on both sides.

a facile hydrothermal procedure was employed to guide the in situ growth of MoS_2 on the graphene sheets in a thiourea solution (Figure 1a). The final product had a well-defined, integrated-film-like morphology (Figure 2a, inset), with dimensions in good agreement with the mold (Figure S1b). Its thickness had significantly increased from 25 μm (for the pristine GO film; Figure S2a) to about 160 μm (Figures S3a and S4a), which is due to the gas release during the reduction of GO by hydrazine vapor.[5f,6] By controlling the addition of

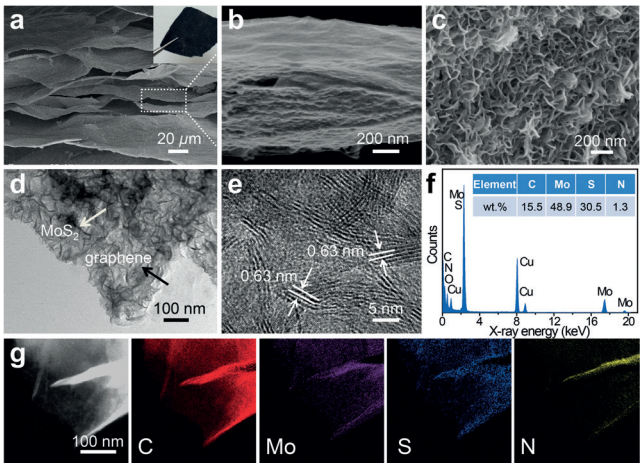

Figure 2. a, b) Different magnifications of cross-sectional SEM images of a NG–MoS_2 film. The inset in (a) shows an optical image of the NG–MoS_2 film. c–e) SEM, TEM, and HRTEM images of the outer surface of a NG–MoS_2 film. f) EDX spectrum of a NG–MoS_2 film. g) Annular dark-field STEM image and the corresponding EDX elemental mappings of C, Mo, S, and N in the NG–MoS_2 film.

the starting materials, the thickness of the film is easily adjustable, and a film thickness of about 250 μm was achieved by simply doubling the amount of added starting materials (Figure S1c, d), indicating that the material preparation is easily scalable. Notably, the composite cross-section showed a foam-like architecture with graphene nanofilms building an interconnected porous structure at the micrometer level, as confirmed by SEM imaging (Figure 2a and Figure S3a, b). A higher-resolution SEM image (Figure 2b) of the indicated area (white dotted rectangle) in Figure 2a surprisingly showed that the seemingly independent graphene nanofilm was actually composed of tens of graphene nanosheets in a densely packed, layered arrangement at the nanoscale. Both SEM and TEM imaging (Figure 2c and d) confirmed that the outer surfaces of the graphene films had been fully covered with honeycomb-like MoS_2 sheets. Furthermore, the graphene nanosheets inside the film were also decorated with nano-MoS_2, forming a layer-by-layer structure at the nanoscale (Figure S3c, d). A film–foam–film architecture was thus formed (Figure 1b, c). The typical lamellar structure of MoS_2 with a few layers (< 5 layers) was confirmed by the ordered lattice fringes of 0.63 nm, which correspond to the interlayer spacings of the (002) planes (see the HRTEM image in Figure 2e). The EDX analysis in Figure 2f revealed the coexistence of C, N, Mo, and S in NG–MoS_2. The content ratio of Mo and S matched the MoS_2 stoichiometry, and a MoS_2 content of 79.4 wt% was calculated from the above EDX data, which approaches the value (84 wt%) calculated from the TGA data in Figure S5. The EDX elemental mappings in Figure 2g further confirmed the complete coverage of the graphene sheets with MoS_2 with homogeneous spatial distributions of C, N, Mo, and S over the surveyed range in the STEM image.

A survey XPS spectrum (Figure S6) provided direct evidence for the presence of C, N, Mo, and S in NG–MoS_2. The chemical states of C, Mo, and S were further analyzed by high-resolution XPS spectroscopy (Figure S7). The C–O–C peak in the C 1s spectrum indicates the presence of a trace amount of oxygen in the NG after reduction (Figure S7a). The binding energies of Mo $3d_{3/2}$ and Mo $3d_{5/2}$ of 232.3 and 229.1 eV are related to the Mo^{4+} ion in MoS_2 (Figure S7c). Although the N 1s and Mo 3p spectra partially overlapped, a distinct N 1s peak could still be observed at 401.7 eV (Figure S7b), and was assigned to the coordination interactions between the MoS_2 nanosheets and the N species in the NG.[7] This interaction promotes the controllable growth and immobilization of MoS_2 on the graphene sheets. The two prominent peaks of S $2p_{1/2}$ and S $2p_{3/2}$ at 163.2 and 162.0 eV in the core-level S 2p XPS spectrum are due to the S^{2-} in MoS_2 (Figure S7d). The XRD pattern in Figure 3a showed distinct (002), (100), (006), and (110) diffraction peaks for MoS_2 (the (006) plane showed a small bump at about 45°), which strongly supported the formation of a hexagonal crystalline MoS_2 2H phase. Furthermore, the characteristic (002) diffraction peak of graphene at 26.6° was not observed, which indicated that the graphene sheets did not restack as they are spaced by MoS_2 interlayers. Raman spectra were recorded to further reveal the microstructures of the NG–MoS_2 composite (Figure 3b). For bulk MoS_2, the two distinct Raman peaks at

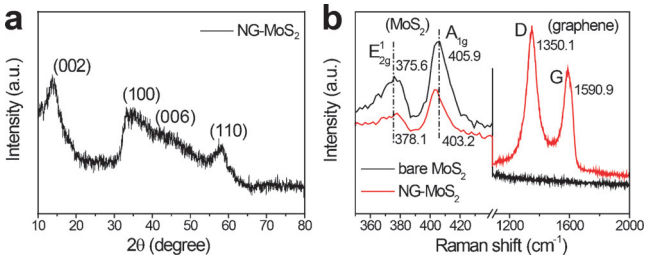

Figure 3. a) XRD pattern of NG–MoS_2. b) Raman spectra of bare MoS_2 and NG–MoS_2.

375.6 and 405.9 cm^{-1} were ascribed to the typical E^1_{2g} and A_{1g} modes of the hexagonal MoS_2 crystal, respectively.[8] In NG–MoS_2, the above two peaks belonging to MoS_2 were shifted to 378.1 and 403.2 cm^{-1}. In particular, the corresponding frequency difference between the E^1_{2g} and A_{1g} mode decreased to 25.1 cm^{-1} compared with 30.3 cm^{-1} for bulk MoS_2, which corroborated the hypothesis that the thickness of the MoS_2 nanosheets had been significantly reduced;[9] this finding is consistent with the HRTEM image in Figure 2e. The other two peaks centered at 1350.1 and 1590.9 cm^{-1} were attributed to the D and G bands of carbon, and the higher intensity of the D band is indicative of the increase in the number of defect sites of graphene during the chemical reduction process.[10]

To highlight the structural characteristics of NG–MoS_2, two control materials were prepared with different synthetic routes. The first control material, denoted as NG/MoS_2, was fabricated by a hydrothermal treatment of an $(NH_4)_6Mo_7O_{24}$-incorporating GO film followed by reduction with hydrazine vapor to yield the final product. The as-obtained NG/MoS_2 film showed a denser structure, and its average thickness was about 90 μm (Figure S8a), which is much smaller than that of NG–MoS_2. This result clearly indicated the influence of the reaction sequence on the microstructure of the product. The core-level C 1s XPS spectra of the NG/MoS_2 film after the hydrothermal treatment but before hydrazine vapor reduction showed the dominant C(sp^2) species at 284.7 eV, suggesting effective removal of oxygen-containing groups in GO in the initial hydrothermal step (Figure S9). The gas-releasing foaming effect of the hydrazine vapor reduction on NG/MoS_2 was negligible, which was believed to lead to the compact structure of the NG/MoS_2 film. Although a layer of MoS_2 was found to have grown on the outer surface of the NG/MoS_2 film (Figure S8b), only a small amount of MoS_2 was seen on the graphene nanosheets inside the composite film (Figure S8c). This could be attributed to the absence of a foam microstructure and the tightly stacked graphene nanosheets in the NG/MoS_2 film, which hinders the in situ growth of MoS_2 inside the film. As a result, the NG/MoS_2 film had a MoS_2 content of 69.2 wt% according to TGA (Figure S5), which is significantly lower than that of the NG–MoS_2 film. The XRD pattern (Figure S10) also confirmed the presence of MoS_2 in NG/MoS_2. Raman spectroscopy revealed the presence of ultrathin MoS_2 nanosheets in the NG/MoS_2 film from the significantly decreased frequency difference between the E^1_{2g} and A_{1g} modes compared with that of bulk MoS_2 (Figure S11), which is similar to that of the NG/MoS_2 foam (Figure 2b).

The other control sample, denoted as NG&MoS_2 film, was prepared by direct hydrazine vapor reduction of a GO film containing pre-synthesized MoS_2. Whereas the film showed a compact macrostructure similar to that of NG/MoS_2, its microstructure varied a lot, and disordered, graphene-wrapped MoS_2 nanoarchitectures were observed both in the cross-section and in the surface of the NG&MoS_2 film (Figure S8d–f). Being blocked by the pre-synthesized MoS_2 on the surface of the GO film, the graphene sheets could not fully expand so that the obtained NG&MoS_2 film had the smallest thickness of about 40 μm (Figure S8d–f), and it contained almost the same amount (83.5 wt%, see Figure S5) of MoS_2 as NG–MoS_2, confirming that the NG foam is a favorable matrix for the growth of MoS_2 in our target composite. Whereas the XRD pattern suggested the formation of MoS_2 (Figure S10), the Raman spectra revealed the incorporation of bulk MoS_2 into the NG&MoS_2 film as confirmed by the almost identical peak positions of the E^1_{2g} and A_{1g} modes in NG&MoS_2 and MoS_2 (Figure S11).

The NG–MoS_2 composites were then prepared into working electrodes and assembled into Li half-cells to investigate their electrochemical performance, and the two control materials were also tested for comparison. Figure 4f and Figure S12 show the cycling voltammograms (CVs) of the three composite electrodes. In the first cathodic process of NG–MoS_2 (Figure 4f), a tiny and irreversible reduction peak appeared at approximately 1.85 V (vs. Li^+/Li, the same below), which may be related to the reduction of the remaining oxygen species on graphene.[11] A broad peak at <1.5 V corresponds to Li intercalation into the layered structure of the 2H phase of MoS_2. Another peak at about 0.75 V suggests the formation of a solid electrolyte interface, which is an irreversible process so that the peak was not observed in the second CV scan.[12] A strong peak at 0.5 V corresponds to the conversion of MoS_2 with intercalated Li into Li_2S and Mo at the end of the discharge (which is also irreversible so that the peak gradually disappeared after 5 CV scans), and the sloped profile at <0.3 V confirmed Li uptake by the NG.[3a,5f] In the reverse anodic scan, two oxidation peaks at 1.51 V and 1.78 V were separately associated with the stepwise oxidation from Mo to Mo^{4+} and further to Mo^{6+} according to previous work while another peak at 2.24 V corresponds to Li deintercalation from the sulfides.[3a] The CV profiles became highly consistent from the second scan, leaving a broad reduction peak centered at about 1.45 V corresponding to the above three oxidation peaks (together, they denote the redox reactions of Mo^{6+}/Mo and sulfides) and a cathodic slope at <0.3 V for the reversible Li intercalation into the NG (Figure 4f).

The two control samples showed similar electrochemistry to NG–MoS_2 judging from the CVs, yet they displayed distinct features (Figure S12). The NG/MoS_2 film gave a small and irreversible reduction peak at 2.3 V during the initial cathodic scan (Figure S12a), which suggested the presence of sulfur in the composite as confirmed by the S 2p XPS spectra (Figure S7e). Owing to the lower MoS_2 loading, the reduction peaks at about 1.5 and 0.5 V in the initial scan, which

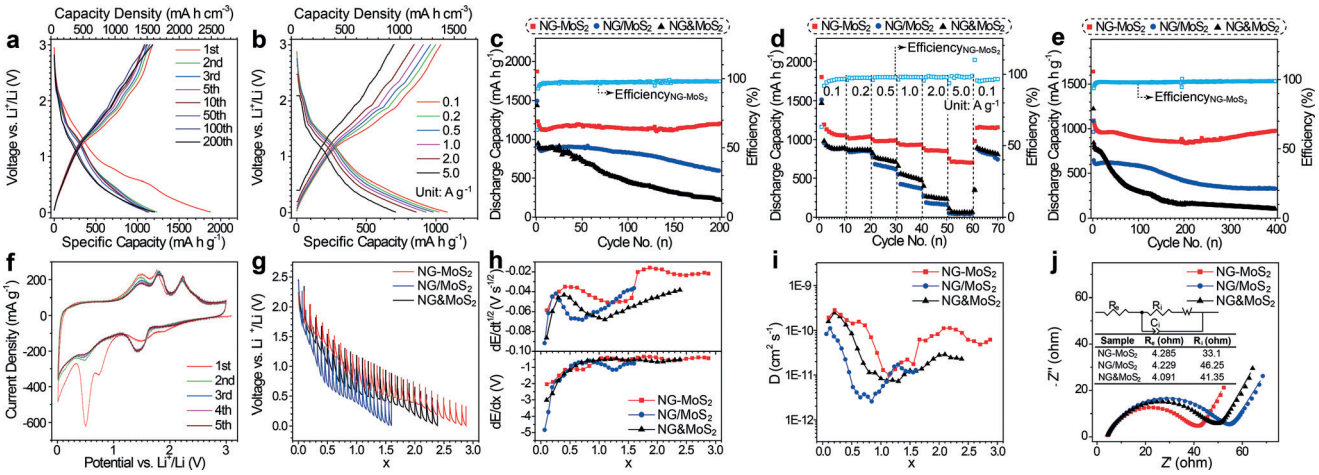

Figure 4. Electrochemical performance and kinetic analysis of the three composite working electrodes in Li half-cells. a) GDC profiles at 0.1 Ag^{-1}. b) GDC profiles at various current densities. c) Cycling performance at 0.1 Ag^{-1}. d) Cycling performance at various current densities. e) Extended cycling performance at 1.0 Ag^{-1}. f) CV profiles of the NG–MoS_2 electrode (scan rate: 0.1 mVs^{-1}). g) GITT profiles ("*x*" denotes the stoichiometry of intercalated Li^+ per mole of composite). h) Calculated values of dE/dx and $dE/dt^{1/2}$ of the NG–MoS_2, NG/MoS_2, and NG&MoS_2 cathodes as a function of stoichiometry. i) Calculated Li chemical diffusion coefficients as a function of the stoichiometry from GITT. j) EIS spectra; the solid lines show fitted curves.

correspond to the Li insertion and conversion reaction of MoS_2, were significantly weakened compared with those measured for NG–MoS_2. In the subsequent scans, the anodic and cathodic peaks denoting the electrochemical redox reaction of MoS_2 were weakened accordingly (Figure S12a). Meanwhile, the compact structure made it difficult for the electrolyte to access the carbon component, which led to the almost complete disappearance of the reduction peak at 1.85 V in the initial cathodic scan and attenuated the slope at <0.3 V. Although NG&MoS_2 has the same MoS_2 content as NG–MoS_2 without the coexistence of sulfur (Figure S7f), the CV peaks of its MoS_2 component were attenuated remarkably (Figure S12b), which could be ascribed to the reduced electrochemical activity of MoS_2 owing to the increased sheet thickness.

The electrochemical performance of the three composites in Li half-cells is summarized in Figure 4. When galvanostatically discharged and charged (GDC) at a low current density of 0.1 Ag^{-1}, NG–MoS_2 displayed an ultrahigh discharge capacity of 1875 $mAhg^{-1}$ and a reasonable Coulombic efficiency (CE) of 63% in the initial cycle (Figure 4a,c) whereas the control samples merely delivered discharge capacities of 1496 $mAhg^{-1}$ (NG/MoS_2) and 1437 $mAhg^{-1}$ (NG&MoS_2). In the subsequent cycles, NG–MoS_2 maintained its capacity advantage over the control samples, with highly consistent GDC profiles observed from the second cycle (Figure 4a), and a reversible capacity of 1205 $mAhg^{-1}$ was achieved after 200 cycles (Figure 4c), which is more than twice as large as that of NG/MoS_2 (593 $mAhg^{-1}$) and five times larger than that of NG&MoS_2 (220 $mAhg^{-1}$). The NG–MoS_2 composite also exhibited improved rate performance. When gradually elevating the current density from 0.1 Ag^{-1} to 5.0 Ag^{-1}, the GDC profiles at each rate remained stable, so that the composite could keep a reversible capacity of about 710 $mAhg^{-1}$ at 5.0 Ag^{-1}, that is, about 64% of its capacity at 0.1 Ag^{-1} (Figure 4b,d). In contrast, NG/MoS_2 and NG&MoS_2 merely delivered about 45 $mAhg^{-1}$ and approximately 60 $mAhg^{-1}$ at 5.0 Ag^{-1}, respectively (Figure 4d). Moreover, when reducing the current density back to 0.1 Ag^{-1}, the capacity of NG–MoS_2 quickly increased to about 1150 $mAhg^{-1}$, suggesting good capacity recovery (Figure 4d). In an extended GDC test at 1.0 Ag^{-1}, NG–MoS_2 demonstrated a CE of about 100% for each cycle and an excellent capacity retention of 980 $mAhg^{-1}$ after 400 cycles (Figure 4e), far beyond the reversible capacities delivered by NG/MoS_2 (330 $mAhg^{-1}$) and NG&MoS_2 (103 $mAhg^{-1}$).

The kinetic advantages and the stable electrochemistry of NG–MoS_2 over the control samples can be linked to its unique 3F structure (Figure 1b). First, the film-like macrostructure ensures structural integrity and leads to high mechanical strength, a precondition for its stable electrochemistry. As shown in Figure S13a, the NG–MoS_2 anode still maintained its intact morphology after 200 GDC cycles at 1.0 Ag^{-1}, with a large amount of S detected (Figure S13a, inset). This result is in sharp contrast with the pulverized morphologies on the NG/MoS_2 and NG&MoS_2 anode after cycling (Figure S13b,c).

Second, the microscopy NG foam skeleton generated by the gas-releasing reduction process provides the necessary spacing for uniform in situ growth of MoS_2 on both sides of single-layer graphene inside the graphene film while also preventing the overgrowth of MoS_2 into bulk materials on the outer surface of the graphene film. When used in a battery, such a microstructure favors the rapid access of Li^+ to the surface of active MoS_2, and more importantly allows the composite to be compressed so that it can reach a higher compact density. As shown in Figure S4b, the NG–MoS_2 film with an initial thickness of about 160 μm can be easily compressed to approximately 60 μm in thickness. In this way, the compact density of NG–MoS_2 can reach 1.32 gcm^{-3}, which is much higher than the compact densities of the two control samples (Table S1). Based on the above compact

density, the NG–MoS_2 composite can deliver a high volumetric capacity density of approximately 1500 $mA\,h\,cm^{-3}$ at 0.1 $A\,g^{-1}$ and maintain 950 $mA\,h\,cm^{-3}$ at 5.0 $A\,g^{-1}$ (Figure 4a,b); these values are significantly higher than the theoretical volumetric capacity density of a graphite anode (818 $mA\,h\,cm^{-3}$, calculated based on its theoretical specific capacity of 372 $mA\,h\,g^{-1}$ and an average density of 2.20 $g\,cm^{-3}$). Moreover, mercury porosimetry analysis of NG–MoS_2 further revealed a total porosity of 69.6% (Figure S14), which means that theoretically, a maximum compression of about 70% can be achieved for the NG–MoS_2 composite so that the energy density can be further increased.

Furthermore, the honeycomb-like MoS_2 structure is firmly anchored onto the surface of NG to form a film at the nanoscopic scale, which enables a direct contact with the highly conductive graphene to facilitate electron transmission. Furthermore, the nitrogen content was found to be directly related to the battery performance of NG–MoS_2, and a low N content achieved by shortening the duration of the hydrazine reduction leads to much worse battery performance (Figure S15 and Table S2). On the other hand, the pinning of MoS_2 also prevents sulfide aggregation and pulverization in the lithiation/delithiation process. As a result, honeycomb-like MoS_2 nanoarchitectures can still be found on the NG–MoS_2 anode after 200 cycles (Figure S12d), confirming its favorable electrochemical stability.

To corroborate the kinetic advantages of the NG/MoS_2 anode, we employed a galvanostatic intermittent titration technique (GITT) to analyze the Li intercalation of the three anodes (Table S3 and Figure 4g–i). According to the GITT profiles, the NG–MoS_2 anode had the highest amount of intercalated Li^+ per mole of composite among the three samples, indicating the largest Li intercalation capacity (Figure 4g). The apparent chemical diffusion coefficient (D_{app}) of Li^+ as a function of x was also calculated for the three anodes according to the GITT results. Whereas similar trends were observed for these samples, the D_{app} value of the NG–MoS_2 anode was significantly higher than those of the control samples, confirming its Li^+ diffusion to be fastest (Figure 4h,i). Furthermore, the electrochemical impedance spectra collected for the three samples indicated that the NG–MoS_2 anode had the lowest charge-transfer resistance, thus demonstrating the optimal electrical contact between NG and MoS_2 in this architecture (Figure 4j). It was also observed that Li^+ diffusion and charge transfer were faster in the NG&MoS_2 anode than in NG/MoS_2 (Figure 4i,j), which agrees with the rate performance results described above (Figure 4d,e). However, the oversized MoS_2 displayed unstable electrochemistry, leading to a quick fading of the capacity of NG&MoS_2 (Figure 4d,e).

In summary, we have described the rational design and scalable assembly of free-standing MoS_2–graphene composite films consisting of N-doped graphene and ultrathin honeycomb-like MoS_2 by combining hydrazine vapor reduction with a hydrothermal reaction. The composite shows a unique hierarchical 3F top-down architecture from the macroscopic to the microscopic and the nanoscopic scale, which improves the diffusion of Li^+ in the composite while also providing a continuous electrical contact from the current collector to the active material, helping accommodate the volume variation upon cycling, and diminishing the excess interface between electrode and electrolyte. The structural merits lead to a high, reversible Li storage capacity of 1200 $mA\,h\,g^{-1}$, an excellent rate capability of 700 $mA\,h\,g^{-1}$ at 5.0 $A\,g^{-1}$, and a very long lifetime of 400 cycles with 980 $mA\,h\,g^{-1}$ retained. From Table S4, it is clear that our NG–MoS_2 anode represents a highly competitive candidate in terms of capacity output.

The preparation method in this work is facile and easily scalable, and the design concept is simple, yet inspiring. Given its significant capacity advantage over traditional anode materials such as graphite, our composite anode material is appealing for high-energy-density batteries, and might contribute to better economic sustainability.

Acknowledgements

This work was supported by the National Natural Science Foundation of China (21571046, 21403050, 21521001, and 21431006), the Program for New Century Excellent Talents in University (2013JYXR0654), the Fundamental Research Funds for the Central Universities (JZ2016HGPA0735, J2014HGBZ0126, and 2014HGQC0015), and the Anhui Provincial Natural Science Foundation (1608085MB32). The electrochemistry study, including GITT and EIS, was supported by the U.S. Department of Energy, Office of Basic Energy Sciences, Division of Materials Sciences and Engineering (DE-SC0005397). We also thank Dr. Shaofei Wang for helpful discussions.

Keywords: composite materials · electrocatalysis · graphene · molybdenum disulfide · nitrogen doping

How to cite: *Angew. Chem. Int. Ed.* **2016**, *55*, 12783–12788
Angew. Chem. **2016**, *128*, 12975–12980

[1] a) Z. Yang, J. Zhang, M. C. W. Kintner-Meyer, X. Lu, D. Choi, J. P. Lemmon, J. Liu, *Chem. Rev.* **2011**, *111*, 3577; b) P. G. Bruce, B. Scrosati, J.-M. Tarascon, *Angew. Chem. Int. Ed.* **2008**, *47*, 2930; *Angew. Chem.* **2008**, *120*, 2972; c) B. Scrosati, J. Hassoun, Y.-K. Sun, *Energy Environ. Sci.* **2011**, *4*, 3287.

[2] a) T. Stephenson, Z. Li, B. Olsen, D. Mitlin, *Energy Environ. Sci.* **2014**, *7*, 209; b) P. P. Wang, H. Sun, Y. Ji, W. Li, X. Wang, *Adv. Mater.* **2014**, *26*, 964; c) H. S. S. Ramakrishna Matte, A. Gomathi, A. K. Manna, D. J. Late, R. Datta, S. K. Pati, C. N. R. Rao, *Angew. Chem. Int. Ed.* **2010**, *49*, 4059; *Angew. Chem.* **2010**, *122*, 4153; d) F. Xiong, Z. Cai, L. Qu, P. Zhang, Z. Yuan, O. K. Asare, W. Xu, C. Lin, L. Mai, *ACS Appl. Mater. Interfaces* **2015**, *7*, 12625; e) X. Zhou, L.-J. Wan, Y.-G. Guo, *Chem. Commun.* **2013**, *49*, 1838; f) X. Fang, X. Guo, Y. Mao, C. Hua, L. Shen, Y. Hu, Z. Wang, F. Wu, L. Chen, *Chem. Asian J.* **2012**, *7*, 1013.

[3] a) F. Zhou, S. Xin, H.-W. Liang, L.-T. Song, S.-H. Yu, *Angew. Chem. Int. Ed.* **2014**, *53*, 11552; *Angew. Chem.* **2014**, *126*, 11736; b) X.-Y. Yu, H. Hu, Y. Wang, H. Chen, X. W. Lou, *Angew. Chem. Int. Ed.* **2015**, *54*, 7395; *Angew. Chem.* **2015**, *127*, 7503; c) J. M. Jeong, K. G. Lee, S. J. Chang, J. W. Kim, Y. K. Han, S. J. Lee, B. G. Choi, *Nanoscale* **2015**, *7*, 324; d) C. Zhu, X. Mu, P. A. van Aken, J. Maier, Y. Yu, *Adv. Energy Mater.* **2015**, *5*, 1401170.

[4] a) A. K. Geim, K. S. Novoselov, *Nat. Mater.* **2007**, *6*, 183; b) D. Kong, H. He, Q. Song, B. Wang, W. Lv, Q.-H. Yang, L. Zhi, *Energy Environ. Sci.* **2014**, *7*, 3320; c) K. Chang, W. Chen, *ACS*

Nano **2011**, *5*, 4720; d) S. Han, Y. Zhao, Y. Tang, F. Tan, Y. Huang, X. Feng, D. Wu, *Carbon* **2015**, *81*, 203; e) L. Ma, J. Ye, W. Chen, D. Chen, J. Yang Lee, *Nano Energy* **2014**, *10*, 144; f) K. Chang, D. Geng, X. Li, J. Yang, Y. Tang, M. Cai, R. Li, X. Sun, *Adv. Energy Mater.* **2013**, *3*, 839.

[5] a) J. Wang, J. Liu, D. Chao, J. Yan, J. Lin, Z. X. Shen, *Adv. Mater.* **2014**, *26*, 7162; b) X. Cao, Y. Shi, W. Shi, X. Rui, Q. Yan, J. Kong, H. Zhang, *Small* **2013**, *9*, 3433; c) Y. Gong, S. Yang, L. Zhan, L. Ma, R. Vajtai, P. M. Ajayan, *Adv. Funct. Mater.* **2014**, *24*, 125; d) W. Wei, S. Yang, H. Zhou, I. Lieberwirth, X. Feng, K. Muellen, *Adv. Mater.* **2013**, *25*, 2909; e) X. Cao, B. Zheng, X. Rui, W. Shi, Q. Yan, H. Zhang, *Angew. Chem. Int. Ed.* **2014**, *53*, 1404; *Angew. Chem.* **2014**, *126*, 1428; f) H.-P. Cong, S. Xin, S.-H. Yu, *Nano Energy* **2015**, *13*, 482; g) H.-P. Cong, J.-F. Chen, S.-H. Yu, *Chem. Soc. Rev.* **2014**, *43*, 7295.

[6] Z. Q. Niu, J. Chen, H. H. Hng, J. Ma, X. D. Chen, *Adv. Mater.* **2012**, *24*, 4144.

[7] H. Tang, J. Wang, H. Yin, H. Zhao, D. Wang, Z. Tang, *Adv. Mater.* **2015**, *27*, 1117.

[8] Y. Li, H. Wang, L. Xie, Y. Liang, G. Hong, H. Dai, *J. Am. Chem. Soc.* **2011**, *133*, 7296.

[9] a) C. Lee, H. Yan, L. E. Brus, T. F. Heinz, J. Hone, S. Ryu, *ACS Nano* **2010**, *4*, 2695; b) H. Li, Q. Zhang, C. C. R. Yap, B. K. Tay, T. H. T. Edwin, A. Olivier, D. Baillargeat, *Adv. Funct. Mater.* **2012**, *22*, 1385.

[10] H.-P. Cong, X.-C. Ren, P. Wang, S.-H. Yu, *Energy Environ. Sci.* **2013**, *6*, 1185.

[11] S. W. Lee, N. Yabuuchi, B. M. Gallant, S. Chen, B.-S. Kim, P. T. Hammond, Y. Shao-Horn, *Nat. Nanotechnol.* **2010**, *5*, 531.

[12] a) Y. Yan, Y.-X. Yin, S. Xin, Y.-G. Guo, L.-J. Wan, *Chem. Commun.* **2012**, *48*, 10663; b) S.-H. Yu, L. Song, S. Xin, H.-Q. Li, D.-W. Xu, H.-P. Cong, *ChemNanoMat* **2016**, *2*, 540.

Received: July 15, 2016
Revised: August 14, 2016
Published online: September 4, 2016

